JOURNAL OF SPACECRAFT AND ROCKETS
Vol. 45, No. 2, March–April 2008

# Flow Control Over a Backward-Facing Step with Application of a Magnetic Field

Ovais U. Khan* and Klaus A. Hoffmann†
*Wichita State University, Wichita, Kansas 67260-0044*

DOI: 10.2514/1.30097

**High-speed flows over a backward-facing step that is subject to an applied magnetic field are numerically simulated. The global domain of computation has been decomposed into upstream and downstream domains from the step location. The low magnetic Reynolds number approximation under a multiblock grid approach is used for modeling the backstep flow. Flux-vector splitting for the convective terms and central differencing for the diffusion terms are used. A time-explicit multistage Runge–Kutta scheme for time integration is implemented. Pressure distribution for the Navier–Stokes analysis is found to be in good agreement with the experimental data. Different types of magnetic field distributions are investigated. Both uniform and variable electrical conductivity distributions have been considered. It has been observed that an increase in the separation zone and displacement of oblique shock wave toward the exit section occurs subsequent to application of the magnetic field. Comparison of results obtained with uniform and variable electrical conductivities has shown a reduction in magnetic interaction for variable electrical conductivity.**

## Nomenclature

$\bar{\mathbf{A}}, \bar{\mathbf{B}}$ = Jacobian matrices
$\boldsymbol{B}$ = magnetic field vector
$\boldsymbol{E}$ = electric field vector
$\mathbf{E} = \{E\}_{\times 1}$ = flux vector component in the $x$ direction
$\mathbf{E}_v = \{E_v\}_{5\times 1}$ = diffusion flux vector in the $x$ direction
$e_t$ = total energy
$\mathbf{F} = \{F\}_{5\times 1}$ = flux vector component in the $y$ direction
$\mathbf{F}_v = \{F_v\}_{5\times 1}$ = diffusion flux vector in the $y$ direction
$\bar{\bar{\mathbf{I}}}$ = identity tensor
$J$ = Jacobian of transformation
$\boldsymbol{J}$ = current density vector
$M$ = Mach number
$p$ = pressure
$\mathbf{Q} = \{Q\}_{5\times 1}$ = field vector
$R_m$ = magnetic Reynolds number
$Re_\infty$ = freestream Reynolds number
$t$ = time
$\boldsymbol{U}$ = velocity vector
$\bar{\mathbf{X}} = \{\bar{X}\}_{5\times 5}$ = right eigenvector matrix associated with $\bar{\mathbf{A}}$
$x, y$ = Cartesian coordinates
$\bar{\mathbf{Y}} = \{\bar{Y}\}_{5\times 5}$ = right eigenvector matrix associated with $\bar{\mathbf{B}}$
$\gamma$ = ratio of specific heats
$\eta$ = generalized coordinate
$\eta_x, \eta_y$ = transformation metrics
$\bar{\mathbf{\Theta}} = \{\bar{\Theta}\}_{5\times 1}$ = flux limiter function vector associated with $\bar{\mathbf{B}}$
$\mu_{e0}$ = free space magnetic permeability
$\xi$ = generalized coordinate
$\xi_x, \xi_y$ = transformation metrics
$\rho$ = density
$\sigma_e$ = electrical conductivity
$\bar{\mathbf{\Phi}} = \{\bar{\Phi}\}_{5\times 1}$ = flux limiter function vector associated with $\bar{\mathbf{A}}$
$\boldsymbol{\nabla}$ = nabla vector

*Subscripts*

$e$ = electromagnetic quantity
$\infty$ = freestream condition

## I. Introduction

SUBSTANTIAL efforts, both experimentally and theoretically, have been devoted to understanding supersonic separated flows over backward-facing steps. At present, research in this area has sufficiently matured to be able to claim that flow separation, flow reattachment, and zones of recirculation have a profound impact on drag and heat-transfer distributions occurring between the wall and the flow. However, both the dynamics and the thermodynamics of this subject are challenging, due to the complex nature of the flow. Nonetheless, the multiplicity of aerospace vehicles and structures exists, about which the external and internal flows often separate; some applications of great interest are supersonic inlets, engine combustors, and flowfield behind blunt nose projectiles and ballistics.

Despite acceptable analytical predictions of total base pressure and drag, these methods cannot predict detailed information about the flowfield. Experimental techniques have always remained popular for providing adequate information about these types of flows. Earlier experimental studies employed conventional measurement techniques for determining pressure, temperature, drag, and heat-transfer rates over backward-facing steps [1]. However, since the late 1980s, classes of nonintrusive optical measurement techniques, for example, laser-induced fluorescence (LIF) [2–4], laser Doppler velocimetry (LDV) [5–7], and particle image velocimetry (PIV) [8] have gained popularity for measuring supersonic separated-flow properties over three-dimensional configurations.

Parallel to experimental efforts, several numerical investigations have been performed to develop a comprehensive theory of supersonic separated flows. Kronzon et al. [9] used finite difference approximation for two-dimensional, steady, viscous supersonic flows over a backward-facing step. Calculations have been performed for a high Reynolds number supersonic flow within a laminar range. Appearance of an expansion fan at the corner, a recompression wake, and a reattachment shock downstream of the step were obvious through the results. They showed that a separation point occurred on the rear wall of the step below the corner. The

---

Presented as Paper 3237 at the 37th Plasmadynamics and Laser Conference, San Francisco, California, 5–8 June 2006; received 30 January 2007; accepted for publication 6 September 2007.

*Graduate Research Assistant, Department of Aerospace Engineering. Student Member AIAA.

†Marvin J. Gordon Distinguished Professor of Aerospace Engineering, Department of Aerospace Engineering. Associate Fellow AIAA.

calculated heat-transfer rates and base pressure were in good agreement with experimental data. Ebrahimi [10] performed a numerical investigation to validate his computational fluid dynamics (CFD) code with the experimental data of [1] for flow over a rearward-facing step. A two-dimensional supersonic flow of perfect gas was considered, and turbulence effects were introduced through the $\kappa$–$\varepsilon$ model. He reported an overprediction in surface pressure at the separation region; however, analysis was in good agreement in the flow-reattachment region. Manna and Chakraborty [11] investigated supersonic flow over unconfined and confined backward-facing steps. They performed a three-dimensional analysis using a commercial CFD solver based on the finite volume approach. The results of both geometries showed evidence of expansion at the corner, a circulation bubble, a reattached shear layer, and a recompressed oblique shock. Their predicted values of pressure, temperature, and velocities were in fair agreement with the experimental data. However, for a confined environment, pressure distribution near the wall region did not agree with the experimental values. They stated that this discrepancy may be due to the ineptness of the turbulence model. It was concluded that despite a complex, reflected shock structure created in confinement, the recirculating flow remained similar to that of the unconfined environment case. Ingelese and Acharya [12] proposed an improved $\kappa$–$\omega$ model for turbulence effects of supersonic compressible flows in a rectangular, backward-facing step channel. It was stated that their improved $\kappa$–$\omega$ model could predict values of skin friction, base pressure, and reattachment length well and in good agreement with the experimental data, as compared to Wilcox's revised $\kappa$–$\omega$ model. It was concluded that the $\kappa$–$\varepsilon$ model of Jones and Launder had deficiencies in modeling these effects. Loth et al. [13] investigated supersonic flows over an axisymmetric, backward-facing step channel for a range of Mach numbers. Their algorithm used adaptive unstructured grids and a shock-capturing scheme that adds a nonlinear contribution through a flux-corrected transport scheme. Euler equations for compressible flow are discretized using the finite element technique. They observed that for an axisymmetric step, the corner expansion wave turns in a downward direction away from the corner, resulting in a relatively weak recompression shock, which does not occur in the two-dimensional cases. The lower-wall surface pressure was in reasonable agreement with the experimental data. Forsythe et al. [14,15] used unstructured and structured grid, implicit, finite volume solvers for modeling turbulence effects over base flows. A detached-eddy simulation for modeling supersonic flows around an axisymmetric base was used. The Spalart–Allmaras, shear stress transport, and Wilcox's $\kappa$–$\omega$ models were implemented. Using an adaptive remeshing algorithm for hybrid grids, Yang [16] investigated supersonic turbulent flow over a backward-facing step. Unsteady mass-averaged Navier–Stokes equations with a two-equation low Reynolds number $\kappa$–$\varepsilon$ turbulence model were computed by a local implicit scheme. First, analyses were performed for an initial unstructured mesh composed of relatively coarse quadrilateral and triangular elements. Regardless of a poor resolution of the flowfield, a successful capturing of an expansion fan and oblique shock wave were evident through initial mesh analyses. Subsequently, an adaptive, refined, unstructured mesh was generated for a second set of numerical experiments, resulting in high-resolution contours. Despite some differences observed in the downstream pressure contours near the upper-wall region of flow, their calculated pressure distributions for a refined mesh agreed well with the experimental data.

A study of plasma dynamics under the influence of electric and magnetic fields has been an area of research in fluid dynamics, which is known as magnetohyrdodynamics (MHD) or magnetofluiddynamics (MFD). Several researchers have shown that magnetic fields can be used to control high-speed flows over various geometries. MacCormack [17–22], Shang et al. [23], Gaitonde and Poggie [24–26], Bityurin et al. [27,28], and Damevin and Hoffmann [29,30] have investigated MHD flows over various geometries, for example, flat plates, channels, blunt bodies, and scramjet engines. An increase in shock standoff distance, a decrease in surface heat transfer, and a decrease in surface static pressure were observed with the application of a particular magnetic field distribution for blunt-body configuration. An increase in thrust and maximum velocity has been reported subsequent to the application of the electromagnetic field for scramjet engines. Recently, Khan et al. [31] investigated the validity of a low magnetic Reynolds number approach for modeling some MFD problems. They reported that this type of formulation can provide accurate results for considerably low values of a magnetic Reynolds number ($R_m \ll 1.0$).

The literature available for this class of flows indicates that few, if any, attempts have been made to explore the effects of an applied magnetic field over backward-facing step flows—the primary objective of the present work. Under a low magnetic Reynolds number approximation, the interaction of an imposed magnetic field with supersonic flow over a two-dimensional backward-facing step has been investigated. Different types of magnetic field distributions have been explored. The governing equations and the numerical schemes are reviewed in the following sections.

## II. Governing Equations

The viscous MFD equations under a low magnetic Reynolds number assumption are as follows:

Continuity equation

$$\frac{\partial \rho}{\partial t} + \boldsymbol{\nabla} \cdot (\rho \boldsymbol{U}) = 0 \tag{1}$$

Momentum equation

$$\frac{\partial (\rho \boldsymbol{U})}{\partial t} + \boldsymbol{\nabla} \cdot [\rho \boldsymbol{U} \otimes \boldsymbol{U} + p \bar{\bar{\mathbf{I}}}] = \boldsymbol{J} \times \boldsymbol{B} + \boldsymbol{\nabla} \cdot \bar{\bar{\boldsymbol{\tau}}} \tag{2}$$

where Ohm's law indicates that

$$\boldsymbol{J} = \sigma_e [\boldsymbol{E} + \boldsymbol{U} \times \boldsymbol{B}] \tag{3}$$

Energy equation

$$\frac{\partial}{\partial t}(\rho e_t) + \boldsymbol{\nabla} \cdot [(\rho e_t + p)\boldsymbol{U}] = \boldsymbol{E} \cdot \boldsymbol{J} + \boldsymbol{\nabla} \cdot (\bar{\bar{\boldsymbol{\tau}}} \cdot \boldsymbol{U}) + \boldsymbol{\nabla} \cdot \boldsymbol{q} \tag{4}$$

where

$$\rho e_t = \frac{1}{2}\rho(u^2 + v^2 + w^2) + \frac{p}{\gamma - 1} \tag{5}$$

These equations are nondimensionalized using the parameters outlined in [29]. The asterisk notation has been dropped, and equations are rearranged in a compact flux-vector formulation as

$$\frac{\partial \mathbf{Q}}{\partial t} + \frac{\partial \mathbf{E}}{\partial x} + \frac{\partial \mathbf{F}}{\partial y} = \frac{\partial \mathbf{E}_v}{\partial x} + \frac{\partial \mathbf{F}_v}{\partial y} + \mathbf{S}_{\mathrm{MFD}} \tag{6}$$

where $\mathbf{Q}$ is the unknown vector, and $\mathbf{E}$, $\mathbf{F}$ and $\mathbf{E}_v$, $\mathbf{F}_v$ are the inviscid and viscous flux vectors, respectively. The additional source term is represented by $\mathbf{S}_{\mathrm{MFD}}$. The nondimensional unknowns, flux vectors, and source terms are provided in Eqs. (7a–7f):

$$\mathbf{Q} = [\rho \quad \rho u \quad \rho v \quad \rho w \quad \rho e_t]^T \tag{7a}$$

$$\mathbf{E} = \begin{bmatrix} \rho u \\ \rho u^2 + p \\ \rho u v \\ \rho u w \\ (\rho e_t + p)u \end{bmatrix} \tag{7b}$$

$$\mathbf{F} = \begin{bmatrix} \rho v \\ \rho v u \\ \rho v^2 + p \\ \rho v w \\ (\rho e_t + p)v \end{bmatrix} \tag{7c}$$

$$\mathbf{E}_v = \frac{1}{Re_\infty}\begin{bmatrix} 0 \\ \tau_{xx} \\ \tau_{xy} \\ \tau_{xz} \\ u\tau_{xx} + v\tau_{xy} + w\tau_{xz} + q_x \end{bmatrix} \tag{7d}$$

$$\mathbf{F}_v = \frac{1}{Re_\infty}\begin{bmatrix} 0 \\ \tau_{yx} \\ \tau_{yy} \\ \tau_{yz} \\ u\tau_{yx} + v\tau_{yy} + w\tau_{yz} + q_y \end{bmatrix} \tag{7e}$$

$$\mathbf{S}_{\mathrm{MFD}} = R_m\begin{bmatrix} 0 \\ (\boldsymbol{J} \times \boldsymbol{B})_x \\ (\boldsymbol{J} \times \boldsymbol{B})_y \\ (\boldsymbol{J} \times \boldsymbol{B})_z \\ (\boldsymbol{J} \times \boldsymbol{B}) \cdot \boldsymbol{U} + \frac{1}{\sigma_e}\boldsymbol{J} \cdot \boldsymbol{J} \end{bmatrix} \tag{7f}$$

where subscripts $x$, $y$, and $z$ indicate vector components in the respective directions. In the present investigation, the applied electric field is set equal to zero, and Newtonian fluid with Stokes hypothesis for the viscous stress terms is used.

The nondimensionalized low magnetic Reynolds number Eq. (6) in physical space $(x, y, z)$ is transformed to a generalized computational space $(\xi, \eta, \zeta)$ and expressed as

$$\frac{\partial \bar{\mathbf{Q}}}{\partial t} + \frac{\partial \bar{\mathbf{E}}}{\partial \xi} + \frac{\partial \bar{\mathbf{F}}}{\partial \eta} = \frac{\partial \bar{\mathbf{E}}_v}{\partial \xi} + \frac{\partial \bar{\mathbf{F}}_v}{\partial \eta} + \bar{\mathbf{S}}_{\mathrm{MFD}} \tag{8}$$

where

$$\bar{\mathbf{Q}} = \frac{\mathbf{Q}}{J} \tag{9a}$$

and

$$\bar{\mathbf{S}}_{\mathrm{MFD}} = \frac{1}{J}\mathbf{S}_{\mathrm{MFD}} \tag{9b}$$

$\bar{\mathbf{E}}$, $\bar{\mathbf{F}}$ and $\bar{\mathbf{E}}_v$, $\bar{\mathbf{F}}_v$ are the inviscid and viscous flux vectors, respectively, in the computational domain. The details of transformed flux vectors have been provided in [32]. Subsequently, the MFD equation (8) can be rewritten by definition of the Jacobian matrices as

$$\frac{\partial \bar{\mathbf{Q}}}{\partial t} + \bar{\mathbf{A}}\frac{\partial \bar{\mathbf{Q}}}{\partial \xi} + \bar{\mathbf{B}}\frac{\partial \bar{\mathbf{Q}}}{\partial \eta} = \frac{\partial \bar{\mathbf{E}}_v}{\partial \xi} + \frac{\partial \bar{\mathbf{F}}_v}{\partial \eta} + \bar{\mathbf{S}}_{\mathrm{MFD}} \tag{10}$$

where details of transformation metrics $\bar{\mathbf{A}}$ and $\bar{\mathbf{B}}$ can be found in [33].

## III. Solution Technique

### A. Multiblock Strategy

Having a physical domain that excludes the upstream region of the step for modeling supersonic backward-facing step flows may not provide accurate results, because even in a supersonic flow, disturbances within the subsonic portion of the boundary layer can travel upstream at the expansion corner and can affect the flowfield. To avoid this negative aspect, it is recommended to include the upstream region of the step. Some advantages of multiblocking include independent grid generation for each block, which alleviates several topological problems encountered in constructing the mesh, a greater control over grid refinement in the regions of interest, savings in computational cost, and economical memory allocation.

Thus, by adopting a multiblock approach in the present analysis, the global physical domain has been decomposed into two subdomains representing upstream and downstream regions with respect to step location. The grid topology of each subdomain remains consistent with the geometry. Subdomains have been connected through common boundaries with a single, overlapped interface. Information will be transferred through a common interface of blocks.

### B. Modified Runge–Kutta Scheme

The modified Runge–Kutta scheme augmented with total variation diminishing (TVD) limiters is used to obtain numerical solutions. The scheme for viscous fluid flow under a low magnetic Reynolds number approach can be expressed as

$$\bar{\mathbf{Q}}_i^{(0)} = \bar{\mathbf{Q}}_i^n \tag{11a}$$

$$\bar{\mathbf{Q}}_{i,j}^{(m)} = \bar{\mathbf{Q}}_{i,j}^n - \frac{\Delta t}{\alpha_m}\left(\frac{\partial \bar{\mathbf{E}}}{\partial \xi} + \frac{\partial \bar{\mathbf{F}}}{\partial \eta} - \frac{\partial \bar{\mathbf{E}}_v}{\partial \xi} - \frac{\partial \bar{\mathbf{F}}_v}{\partial \eta} - \bar{\mathbf{S}}_{\mathrm{MFD}}\right)_{i,j}^{(m-1)} \tag{11b}$$

where $m = 1{:}4$, and $\alpha_m = 4{:}1$. The TVD model, based on the eigenstructure of the flux Jacobian matrices, has been used in the last stage of computation, which is generally known as the postprocessing stage as

$$\begin{aligned}\bar{\mathbf{Q}}_{i,j}^{n+1} = \bar{\mathbf{Q}}_{i,j}^4 &- \frac{1}{2}\frac{\Delta t}{\Delta \xi}[\bar{\mathbf{X}}_{i+1/2,j}^n \bar{\boldsymbol{\Phi}}_{i+1/2,j}^n - \bar{\mathbf{X}}_{i-1/2,j}^n \bar{\boldsymbol{\Phi}}_{i-1/2,j}^n] \\ &- \frac{1}{2}\frac{\Delta t}{\Delta \eta}[\bar{\mathbf{Y}}_{i,j+1/2}^n \bar{\boldsymbol{\Theta}}_{i,j+1/2}^n - \bar{\mathbf{Y}}_{i,j-1/2}^n \bar{\boldsymbol{\Theta}}_{i,j-1/2}^n]\end{aligned} \tag{11c}$$

In the current investigation, a Davis–Yee symmetric TVD scheme is implemented. Details of flux-limiter vectors $\bar{\boldsymbol{\Phi}}$ and $\bar{\boldsymbol{\Theta}}$ are provided in [33]. Eigenvector matrices $\bar{\mathbf{X}}$ and $\bar{\mathbf{Y}}$ corresponding to Euler equations are provided in [32].

## IV. Applications

The basic features of supersonic base flows are depicted in Fig. 1. The complex nature of the flowfield is evident in the vicinity of the backward-facing step that involves formations of an expansion fan at the corner, flow recirculation, a free shear layer, and an oblique shock wave. This complexity of flowfield causes spurious numerical difficulties and affects solution convergence that may not provide correct results. Therefore, an accurate and efficient grid that results in a correct converged solution within a permissible limit of time is necessary. Figure 2 shows a two-dimensional computational grid obtained after several grid independent tests. Grid clustering is enforced at the base and near the wall regions to accurately capture the large flow gradients. The domains upstream and downstream of the step have been specified according to the dimensions provided in [1]. It is important to mention that the difference in pressure values was large at the beginning of the recompression region (closer to the base and near the recirculation corner) for different grid spacing. Thus, more grid points have been introduced at this region to attain better accuracy. Finally, grid spacing of $112 \times 120$ for the

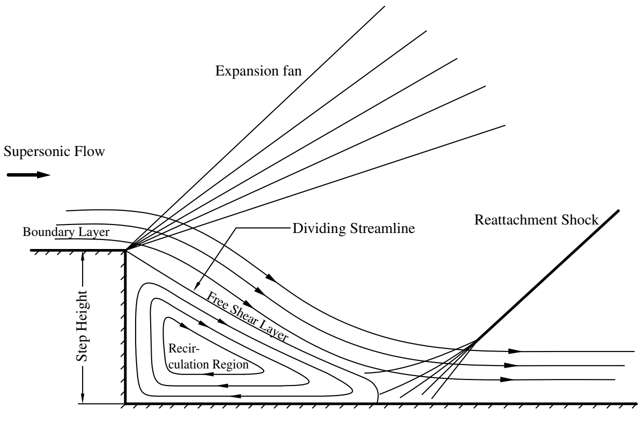

**Fig. 1 Illustration of supersonic flowfield over backward-facing step.**

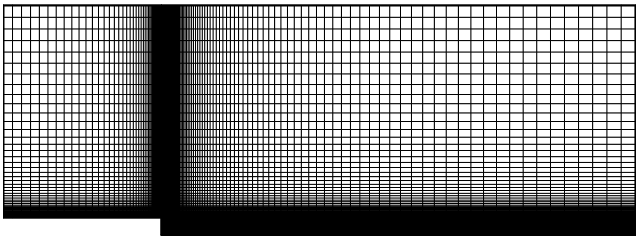

Fig. 2 Multiblock computational grid for the present analysis.

downstream domain and 56 × 61 for the upstream domain have been chosen for all subsequent analyses. The data for investigating the validity of the developed model have been obtained from the experimental work of Smith [1]. Details of the geometry and operating conditions are as follows:

step height = 11.252 mm;
upstream length = 101.6 mm;
downstream length = 304.8 mm;
upstream height = 147.78 mm;
Mach number: $M_\infty = 2.5$;
pressure: $P_{\text{stag}} = 127.553$ kPa;
temperature: $T_{\text{stag}} = 362.44$ K;
$Re_\infty = 1.005 \times 10^4/\text{mm}$.

It should be noted that the experimental data in [1] were provided in foot–pound–second (fps) system which has been converted into SI system of units for the present computations. The current numerical analysis has been performed for flow exposed to an unconfined environment. The term “unconfined environment” refers to the domain of flow that does not contain an upper wall; therefore, an extrapolating boundary condition is required at the upper wall for numerical computation. However, the term “confined environment” considers the upper wall of the domain; thus, a no slip boundary condition is usually specified for the numerical simulation. The developed model has been validated with the experimental data for the Navier–Stokes calculation; subsequently a numerical MFD analysis has been conducted for different magnetic field distributions.

### A. Navier–Stokes Analysis

Figure 3 illustrates pressure contours along with streamlines obtained for the Navier–Stokes computation. Formation of the expansion fan is evident, with the leading expansion wave at approximately 23.8 deg, compared to a value of 23.58 deg obtained from the analytical solution for an inviscid, supersonic flow. A circulation region at the corner that contains a complex structure of vortices is also obvious in the figure; approximately uniform pressure has been observed in this region. Flow separation and reattachment can be observed by considering the streamlines; in fact, a shear layer separates the circulation region from the flow downstream of the expansion fan. Finally, the appearance of an oblique shock wave through coalescence of compression waves further downstream has occurred, which results in turning of the flow parallel to the freestream direction. Moreover, a comparison of the turning angle measured between the shear layer and the wall of the test section has also been made with the experimental value. The flow turning angle from the present numerical computation is found to be approximately 17 deg, which is in agreement with the measured value of 17 deg obtained from the shadowgraph of the experiment reported in [1].

The computed pressure distribution along the horizontal surface downstream of the step is compared to the experimental values of Smith [1] in Fig. 4. A reasonably good agreement between the experimental and numerical values of the pressure has been achieved; freestream pressure is used to nondimensionalize the values.

### B. Magnetofluiddynamic Analysis for Pressure Distribution

Subsequent to validating the developed model, computations have been initiated to investigate the effects of an applied magnetic field for this complex class of flows. Air is assumed to be calorically perfect under laminar flow conditions. Electrical conductivity of gas in the upstream domain is set to zero, while a value of electrical conductivity equal to 1142 Siemens/m is selected in the downstream domain. This value of electrical conductivity has been chosen to achieve a low value of magnetic Reynolds number, such that low magnetic Reynolds number approximation can be used. With this value of electrical conductivity the magnetic Reynolds number based on the step height is equal to 0.01. The load factor is zero; that is, there is no applied electric field. Three types of magnetic field distributions with varying strengths have been implemented for MFD flow control analyses.

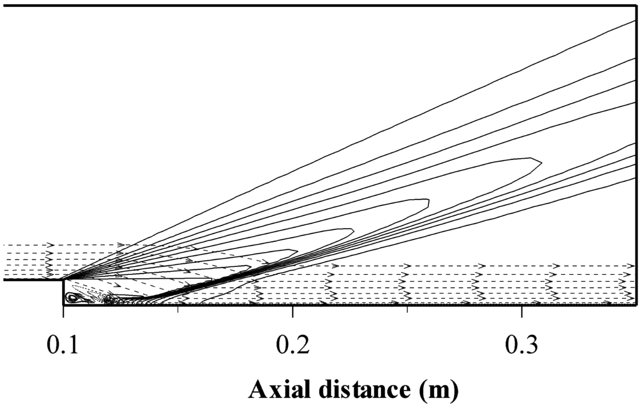

Fig. 3 Pressure contours obtained from the solution of the Navier–Stokes equations.

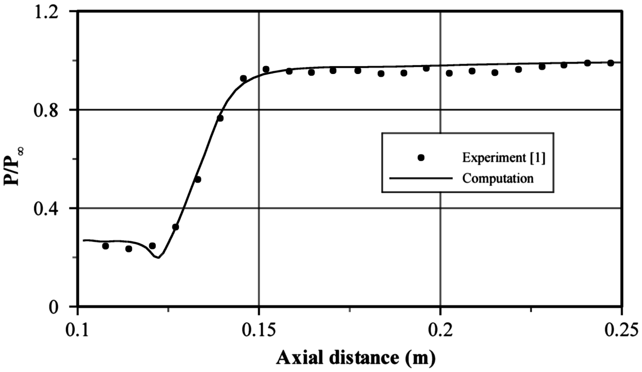

Fig. 4 Comparison of pressure distribution with experimental data of [1].

#### 1. Uniform Magnetic Field in y Direction

The first set of numerical experiments for MFD consists of the application of a uniform magnetic field in the $y$ direction perpendicular to the freestream flow. The magnetic field is attenuated far downstream before exit to prevent flow separation at the exit, which will certainly violate the extrapolating boundary condition and may cause solution divergence. The applied magnetic field has a uniform value from $x = 0.1016$ m to $x = 0.1778$ m and decreases linearly to zero from $x = 0.1778$ m to $x = 0.3302$ m. Figure 5 illustrates the applied magnetic field distribution along with pressure contours obtained with magnetic field strengths of 0.15 and 0.25 T. Comparison with the Navier–Stokes analysis indicates a significant increase in the size of the circulation zone that causes a displacement in the oblique shock-wave location. Furthermore, the oblique shock wave becomes steeper and thicker compared to the Navier–Stokes prediction, following the application of a magnetic field.

Figure 6 represents pressure distributions obtained along the horizontal surface downstream of the step for different magnetic field strengths along with the Navier–Stokes calculation. Comparison with the Navier–Stokes analysis reveals an overall increase in pressure levels and displacement in the shock location toward the

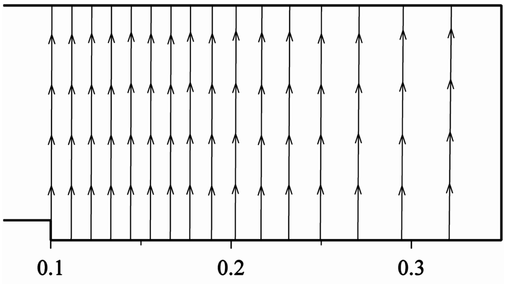

**a) Magnetic field distribution**

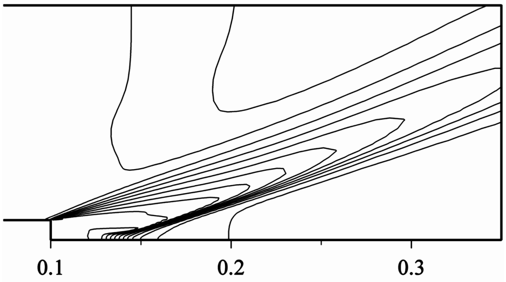

**b) $B_y = 0.15$T**

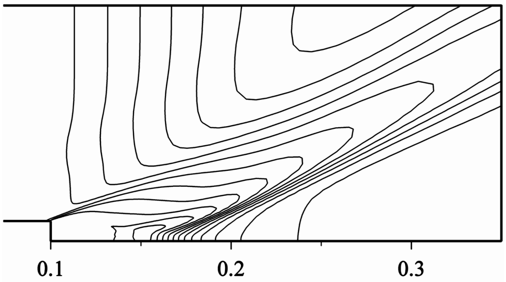

**c) $B_y = 0.25$T**

**Fig. 5 Uniform magnetic field distribution along with pressure contours obtained with different strengths of the magnetic field.**

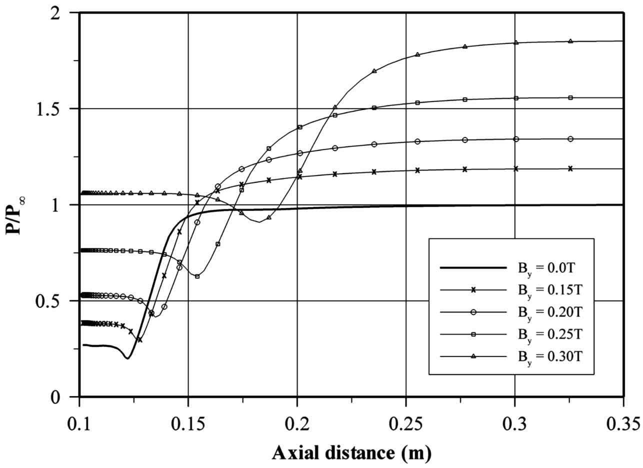

**Fig. 6 Pressure distributions along the horizontal surface for different values of the uniform magnetic field strengths.**

exit section with the increase of applied magnetic field intensity. The magnetic field is causing high pressure downstream of the step over the entire domain; in fact, it is the Lorentz force which results in flow compression and shock standoff in this region. Nonetheless, the pressure difference between upstream and downstream of the shock slightly decreases as observed from Fig. 6. It is interesting to note that although pressure increases after application of the magnetic field, it remains uniform in the recirculation region. Furthermore, a decrease in flow velocity is also observed with the application of a magnetic field. This flow retardation strongly depends on the magnitude of the magnetic field and occurs because of Lorentz force generated as the result of the interaction of plasma and the magnetic field.

### 2. *Magnetic Field Generated by a Dipole Aligned with the x Axis*

The second set of MFD analyses employs two cases of magnetic field distribution generated by placing dipoles aligned with the positive $x$ axis at two different locations of 0.1397 and 0.2032 m in the downstream domain. Figure 7 shows pressure contours along with magnetic field distributions for both dipole locations. For the dipole located at $x = 0.1397$ m, the application of a $B_0 = 1.0$ T magnetic field causes a movement of shock toward the downstream section and a small smearing of the shock. Increase of the magnetic field strength to a value of $B_0 = 2.0$ T further pushes the shock wave toward downstream at the exit section, causes substantial shock smearing, and reduces the expansion fan angle.

For the dipole positioned at $x = 0.2032$ m, the flow structure remains mostly similar to the Navier–Stokes flowfield after the application of a magnetic field of $B_0 = 1.0$ T, except some compression waves have been observed at the dipole location. Nonetheless, further increase of magnetic field strength ($B_0 = 2.0$ T) has not only generated the strong compression waves at the dipole location but also has resulted in the increase of the recirculation zone thus causing a shock displacement toward the exit section. Moreover, shock-smearing, reduction in the expansion fan angle and a slight increase in the shock-wave angle are also observed after the application of a magnetic field of $B_0 = 2.0$ T.

Figure 8 depicts pressure distributions along the horizontal surface downstream of the step for the two locations of dipoles, discussed previously in Fig. 7. A gradual increase in pressure distributions at the circulation region and the movement of shock toward the exit section are evident for MFD analysis with the dipole located at $x = 0.1397$ m. In contrast, for the dipole positioned at $x = 0.2032$ m and application of $B_0 = 1.0$ T the magnetic field neither causes an increase in pressure at the recirculation region nor results in movement of the shock. However, for magnetic field strength of $B_0 = 2.0$ T, a significant rise in pressure at the recirculation zone and displacement of the shock are observed. Moreover, a flow compression phenomenon at the dipole location of $x = 0.2032$ m is also evident for MFD computations; that is, for $B_0 = 1.0$ T, the pressure distribution remains similar to the Navier–Stokes analysis from the base to $x \cong 0.15$ m; however, a rise in pressure at the neighborhood of the dipole position has occurred. Further enlargement in pressure hills has been observed for the magnetic intensity of $B_0 = 2.0$ T. The appearance of pressure hills indicates that magnetic interaction becomes important within the boundary layer at the position where a strong magnetic field is present. In fact, MFD interaction is inversely proportional to the velocity, because velocity within the boundary layer decreases, while magnetic interaction increases. Finally, pressure recovery is achieved for all values of magnetic field strengths at the exit section for both dipole positions.

### 3. *Magnetic Field Generated by a Dipole Pointed in the Direction of the y Axis*

Finally, dipoles with their axes perpendicular to the surface have been placed at two different locations for magnetofluiddynamic computations. Figure 9 indicates the magnetic field generated by dipoles and the corresponding pressure distributions for different field strengths. For the dipole positioned at 0.1397 m in the downstream domain, a displacement of shock toward the exit section and some smearing of the oblique shock wave are observed with a magnetic field of $B_0 = 1.0$ T. Furthermore, an increase of the magnetic field strength ($B_0 = 2.0$ T) causes considerable shock-smearing, shock movement toward the exit section and reduction in the expansion fan angle.

Similar to the previous case of Sec. II, for the dipole located at $x = 0.2032$ m, application of a magnetic field of $B_0 = 1.0$ T has resulted in the formation of a compression wave at the dipole position without causing any changes in oblique shock standoff. However, for $B_0 = 2.0$ T, considerable shock displacement toward the exit section

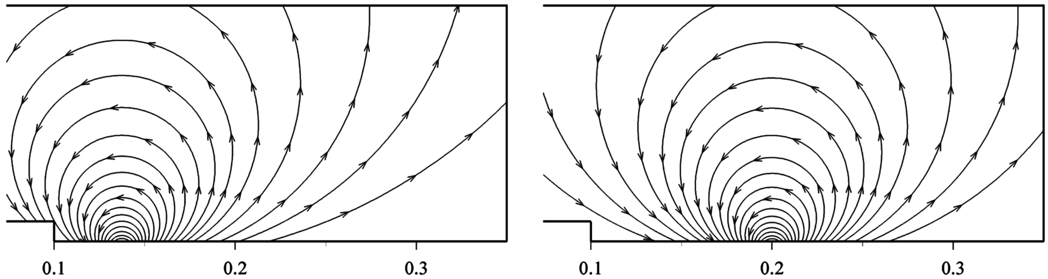

**Dipole at x = 0.1397 m** **Dipole at x = 0.2032 m**

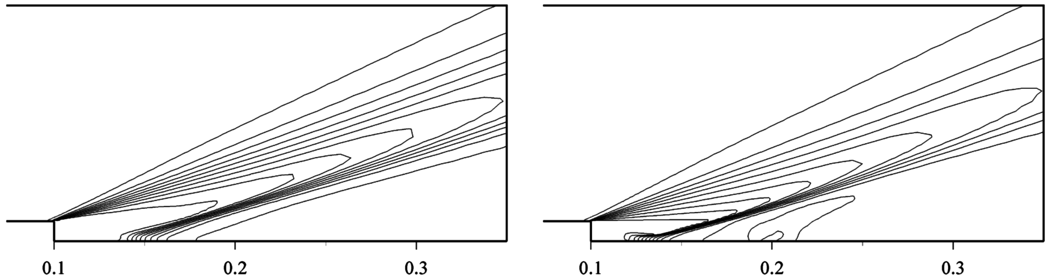

**$B_o$ = 1.0T** **$B_o$ = 1.0T**

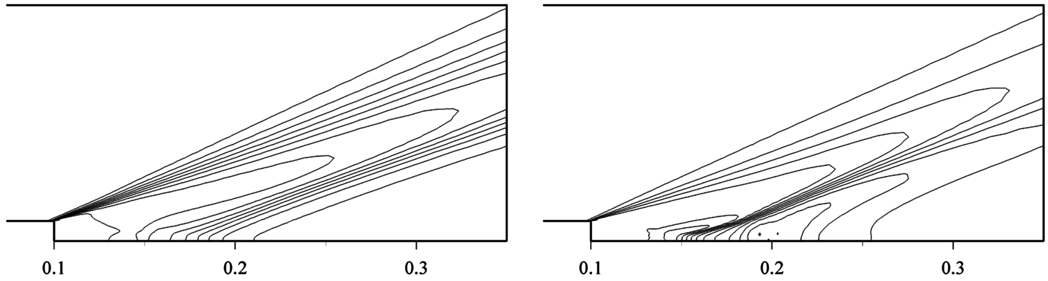

**$B_o$ = 2.0T** **$B_o$ = 2.0T**

**Fig. 7 Magnetic field distributions generated by dipoles aligned with the *x* axis and corresponding pressure contours obtained with different magnetic field strengths.**

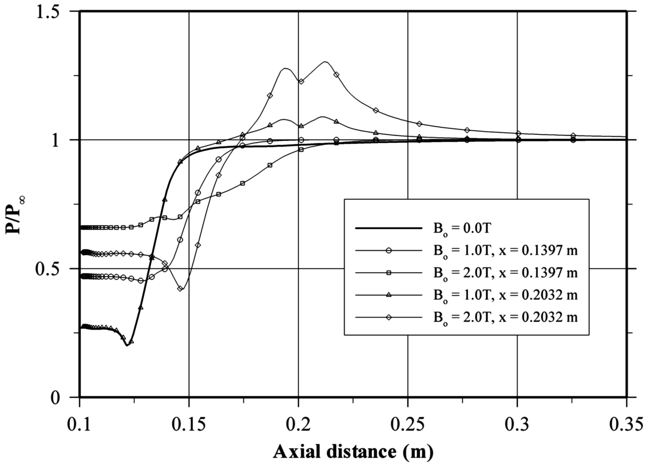

**Fig. 8 Pressure distributions along the horizontal surface for different magnetic field strengths of dipoles aligned with the *x* axis.**

and strong compression waves have been generated at the dipole location. In addition, shock-smearing, reduction in the expansion fan angle and a small increment in the oblique shock-wave angle have occurred for the higher strength of the magnetic field.

Figure 10 shows pressure distributions along the surface for the different dipole locations with different strengths of magnetic field. Shock displacements for both dipole locations discussed earlier are clearly visible in this figure. For the dipole located at $x = 0.1397$ m, the increase in pressure levels at the circulation region has taken place for all values of magnetic fields. Interestingly, the flow expansion that had occurred before the shock for the Navier–Stokes computation has not occurred for MFD computation with a magnetic field strength of $B_0 = 1.0$ T. Moreover, this small expansion for the Navier–Stokes calculation mutates to flow compression with further increase of magnetic field strength ($B_0 = 2.0$ T). Nevertheless, recovery in all pressure levels is achieved downstream of the oblique shock region. For the dipole positioned at $x = 0.2032$ m, the pressure level in the recirculation zone and the shock location remains similar to the Navier–Stokes analysis, except a hill has appeared at the dipole location after crossing the shock wave for the magnetic field of $B_0 = 1.0$ T. However, for $B_0 = 2.0$ T, an increase in pressure at the recirculation region and significant shock displacement have occurred. Furthermore, a substantial rise in the pressure hill has taken place at the dipole location for higher magnetic field intensity which confirms that magnetic interaction has increased in the boundary layer. Again, pressure is becoming uniform downstream of the oblique shock wave for all magnetic field strengths.

### 4. *Effect of the Temperature Dependency of Electrical Conductivity*

In the last part of the MFD analysis, the effect of variable electrical conductivity on MFD control of flow over a backward-facing step has been explored. The expression for electrical conductivity distribution has been taken from [26] and provided here as

$$\sigma_e = \sigma_0 \left( \frac{T}{T_{\text{stag}}} \right)^{4.0}$$

where $\sigma_0$ is the constant value of electrical conductivity and $T_{\text{stag}}$ is the stagnation temperature. Figure 11 shows pressure contours

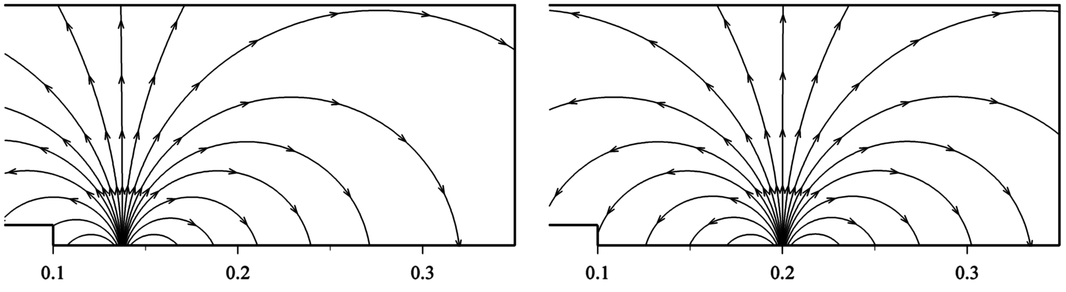

**Dipole at x = 0.1397 m** **Dipole at x = 0.2032 m**

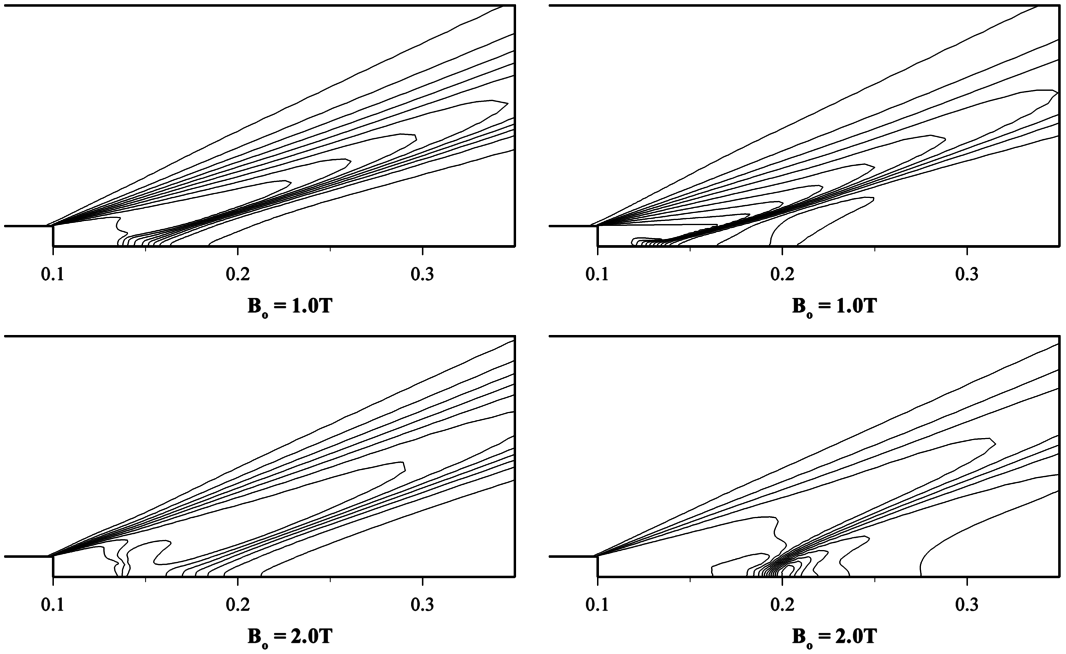

**$B_o$ = 1.0T** **$B_o$ = 1.0T**

**$B_o$ = 2.0T** **$B_o$ = 2.0T**

**Fig. 9 Magnetic field distributions generated by dipoles pointed in the direction of the *y* axis and corresponding pressure contours obtained with different magnetic field strengths.**

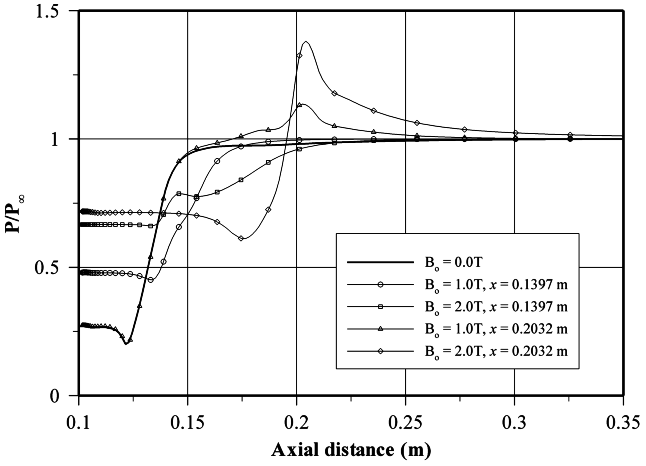

**Fig. 10 Pressure distributions along the horizontal surface for different magnetic field strengths of dipoles pointed in the direction of the *y* axis.**

obtained with uniform magnetic field distribution by considering variable electrical conductivity of the medium. Note that magnetic field strength of 0.25 T is not producing considerable change in the flow structure as observed previously for the constant electrical conductivity case (see Fig. 5c). However, with the increase of magnetic field intensity (0.5 T) enlargement of the recirculation zone, shock smearing and movement of the shock toward the exit section have occurred as depicted in Fig. 11b.

Figure 12 represents pressure distributions obtained along the horizontal surface downstream of the step for the constant and variable electrical conductivities along with the Navier–Stokes analysis. It is worthwhile to observe that for constant electrical conductivity computation the magnetic field of 0.25 T strength has caused a significant rise in the pressure distribution and considerable displacement in the shock location, whereas for the variable electrical conductivity case neither the rise in pressure nor the shock displacement are significant as compared to the Navier–Stokes calculations. The comparison of results obtained with the constant and variable electrical conductivities indicates that a decrease in magnetic interaction has been observed for variable electrical conductivity distribution which will reduce the effectiveness of MFD control.

### C. Velocity Distributions

Figure 13 illustrates streamline patterns for the Navier–Stokes and the MFD flow computations for different magnetic field distributions. The results of highest magnetic field strength for each distribution have been provided to explicitly discuss the influence of the magnetic field. Because these patterns have qualitative representations of the flowfield, an enlarged region near the step corner has been presented to provide a better understanding of the circulation region. Streamlines through a Prandtl–Mayer expansion turn toward the lower surface, and attainment of a freestream direction through the oblique shock wave is visible in all cases. As can be seen from the figure, a complex structure of circulation in the separation bubble is evident in all cases—each one having a distinct shape from the other. A combination of upper and lower vortices has been observed for the present Navier–Stokes and

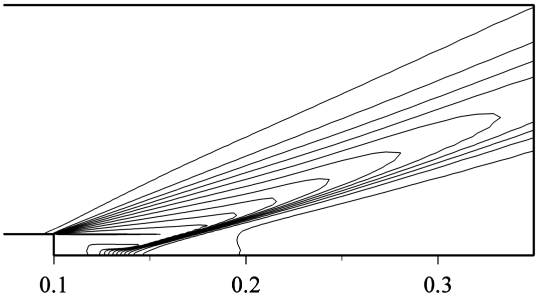

**a) $B_y$ = 0.25T**

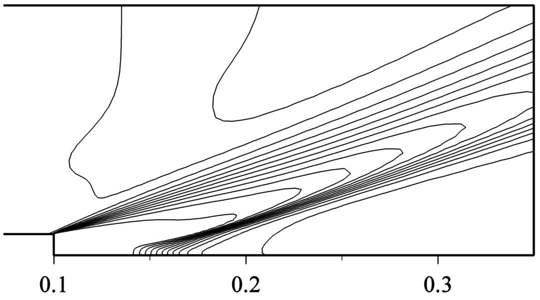

**b) $B_y$ = 0.5T**

**Fig. 11 Pressure contours obtained with variable electrical conductivity for different strengths of uniform magnetic field distribution.**

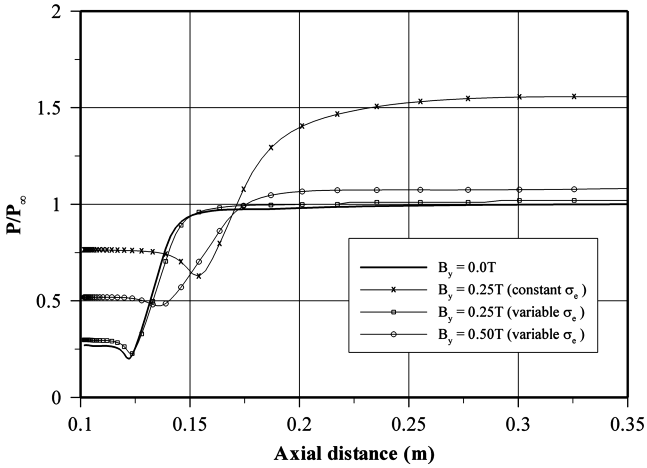

**Fig. 12 Pressure distributions along the horizontal surface for constant and variable electrical conductivity distributions.**

MFD calculations. For convenience, the lower vortex is referred to as the primary vortex, and the upper vortex is referred to as the secondary vortex.

It is interesting to observe that the separation bubble is smaller in size in the Navier–Stokes analysis; application of the magnetic field has caused enlargement in the size of the separation bubble for all distributions. Furthermore, the magnetic effects have changed the vortices' structure within the bubble, as compared to the Navier–Stokes prediction. Relatively smaller vortices are observed for the Navier–Stokes calculations, whereas large vortices have occurred for MFD flow computations, although size and shape of these vortices strongly depend on the orientation and strength of the magnetic field vectors.

For example, in the case of a uniform magnetic field distribution along the *y* direction, enlargement of the separation bubble and a combination of vortices are evident in Fig. 13b. Moreover, the primary vortex located under the secondary vortex has been stretched toward the reattachment point downstream of the step.

Similar characteristic behavior of this vortex topology remains persistent for both orientations of dipoles located at $x = 0.1397$ m and $x = 0.2032$ m in the downstream domain. For the dipole positioned at $x = 0.1397$ m, the magnetic effects have resulted in contraction of the primary vortex confined to the corner and further enlargement of the secondary vortex extended up to the reattachment

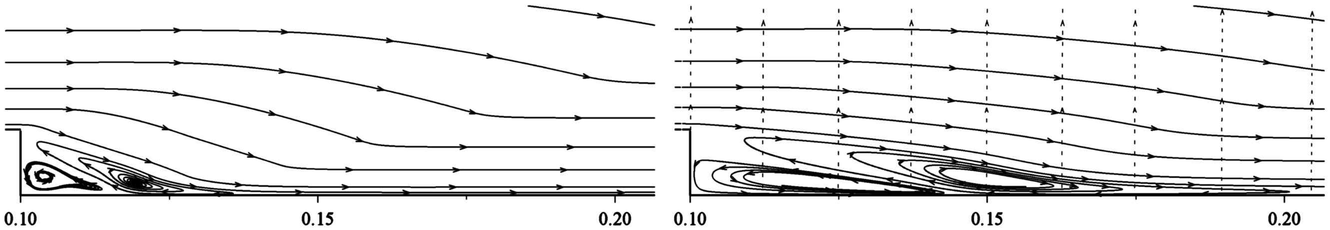

**a) Navier-Stokes**

**b) Uniform magnetic field along the y axis ($B_y$ = 0.25T)**

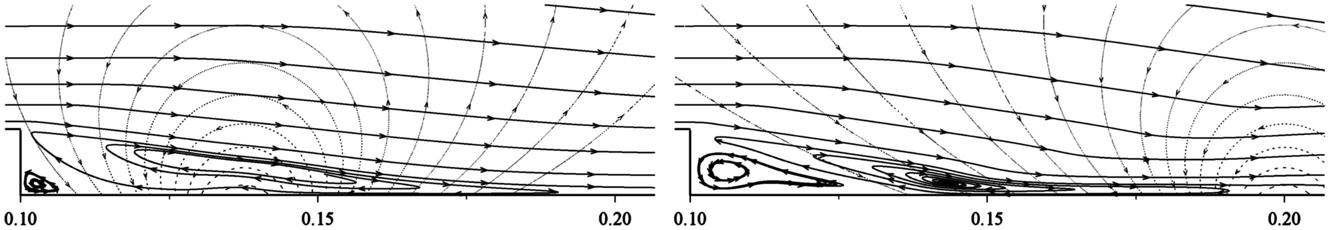

**c) Dipole pointed along the x axis at x = 0.1397 m ($B_o$ = 2.0T)**

**d) Dipole pointed along the x axis at x = 0.2032 m ($B_o$ = 2.0T)**

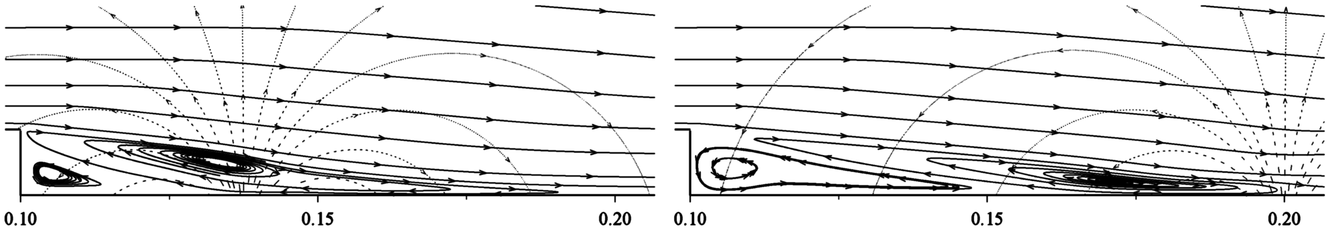

**e) Dipole pointed along the y axis at x = 0.1397 m ($B_o$ = 2.0T)**

**f) Dipole pointed along the y axis at x = 0.2032 m ($B_o$ = 2.0T)**

**Fig. 13 Streamline patterns for the Navier–Stokes and MFD computations with different magnetic field distributions.**

point, as shown in Figs. 13c and 13e, for both dipole orientations along the $x$ and $y$ axes. In contrast, for the dipole located at $x = 0.2032$ m, the magnetic field has resulted in an expansion and stretching of the primary vortex and a small contraction in the secondary vortex, as depicted in Figs. 13d and 13f for both dipole orientations along the $x$ and $y$ axes.

## V. Conclusions

A low magnetic Reynolds number approach has been used to numerically simulate the effects of an applied magnetic field on supersonic separated flows over a backward-facing step. Using a mutliblock solution strategy, a viscous, compressible MFD set of equations has been solved. The numerical scheme is based on a four-stage modified Runge–Kutta scheme with TVD limiters. Different types of magnetic field distributions have been implemented for the MFD computations. Several magnetic field configurations under consideration have caused an increase in the size of the separation bubble, movement of shock toward the exit section, an increase in the oblique shock-wave angle, and a decrease in flow velocity in the plasma domain. Moreover, the applied magnetic field has altered the vortex patterns for all types of magnetic field distributions. A uniform magnetic field has caused an increase in pressure levels downstream of the step over the entire domain. A further increase in the strength of the magnetic field has thickened the oblique shock wave. For the dipole aligned with the positive $x$ axis, flow compression at the recirculation region and shock smearing are observed for $x = 0.1397$ m location. For the dipole positioned at $x = 0.2032$ m, formation of pressure hills in the neighborhood of the dipole position has taken place for MFD computations; however, flow compression at the recirculation region has occurred only for the higher strength of magnetic field. For the dipole pointed in the positive $y$-axis direction, an increase in pressure at the circulation zone and shock smearing have occurred for the $x = 0.1397$ m position. Whereas, for the location of $x = 0.2032$ m, an increase in pressure levels at the circulating region and formation of a pressure hill after crossing the shock at the dipole location are observed with the increase of magnetic field intensity. Computations performed with temperature dependent electrical conductivity distribution have shown a reduction in MFD effects as compared to the constant conductivity case. Interaction of the applied magnetic field with the flow is strongly dependent on distribution of electrical conductivity in the domain, the strength and type of magnetic field distributions, locations, and orientations.

## Acknowledgment

The authors acknowledge the support of the Wichita State University High Performance Computing Center for conducting the computational tasks.

## References

[1] Smith, H. E., “The Flow Field and Heat Transfer Downstream of a Rearward Facing Step in Supersonic Flow,” Aerospace Research Laboratories Paper ARL-67-0056, March 1967.

[2] Fletcher, D. G., and McDaniel, J. C., “Quantitative Measurement of Transverse Injector and Free Stream Interaction in a Nonreacting Scramjet Combustor Using Laser Induced Fluorescence,” AIAA Paper 1987-0087, 1987.

[3] McDaniel, J. C., Fletcher, D. G., Hartfield, R. J., and Hollo, S. D., “Staged Transverse Injection into Mach 2 Flow Behind a Rearward-Facing-Step: A 3-D, Compressible Flow Test Case for Hypersonic Combustor CFD Validation,” AIAA Paper 1992-0827, 1992.

[4] Hartfield, R. J., Hollo, S. D., and McDaniel, J. C., “Planar Measurement Technique for Compressible Flows Using Laser-Induced Iodine Fluorescence,” *AIAA Journal*, Vol. 31, No. 3, 1993, pp. 483–490.

[5] Petrie, H. L., Samimy, M., and Addy, A. L., “A Study of Compressible Turbulent Free Shear Layers Using Laser Doppler Velocimetry,” AIAA Paper 1985-0177, 1985.

[6] Abu-Hijleh, B., and Samimy, M., “An Experimental Study of a Reattaching Supersonic Shear Layer,” AIAA Paper 1989-1801, 1989.

[7] Arai, T., Sugiyama, H., Homareda, M., and Uno, N., “Turbulence Characteristics of Supersonic Boundary Layer Past a Backward Facing Step,” AIAA Paper 1995-6126, 1995.

[8] Kuratani, N., Ikeda, Y., Nakajima, T., Tomioka, S., and Mitani, T., “Mixing Characteristics of Normal Injection into a Supersonic Backward-Facing Step Flow Measured with PIV,” AIAA Paper 2002-0237, 2002.

[9] Kronzon, Y., Rom, J., and Seginer, A., “Laminar Supersonic Flow over a Backstep—A Numerical Solution at Higher Reynolds Numbers,” *25th Proceedings of the Heat Transfer and Fluid Mechanics Institute*, Stanford Univ. Press, Stanford, CA, 21–23 June 1976.

[10] Ebrahimi, H., “CFD Validation and Evaluation for Reacting Flows, Part III,” AIAA Paper 1995-0735, 1995.

[11] Manna, P., and Chakraborty, D., “Numerical Simulation of Supersonic Flow Behind a Backward Facing Step in Free and Confined Environment,” AIAA Paper 2005-3647, 2005.

[12] Ingelese, F., and Acharya, S., “An Improved k-Omega Model for Compressible flows,” AIAA Paper 1996-0428, 1996.

[13] Loth, E., Kailasanath, K., and Löhner, R., “Supersonic Flow Over an Axisymmetric Backward-Facing Step,” *Journal of Spacecraft and Rockets*, Vol. 29, No. 3, May–June 1992, pp. 352–359.

[14] Forsythe, J. R., Hoffmann, K. A., and Dietiker, J. F., “Detached-Eddy Simulation of a Supersonic Axisymmetric Base Flow with an Unstructured Solver,” AIAA Paper 2000-2410, 2000.

[15] Forsythe, J. R., Hoffmann, K. A., and Squires, K. D., “Detached-Eddy Simulation with Compressibility Corrections Applied to a Supersonic Axisymmetric Base Flow,” AIAA Paper 2002-0586, 2002.

[16] Yang, S. Y., “Adaptive Strategy of the Supersonic Turbulent Flow over a Backward-Facing Step,” *International Journal for Numerical Methods in Fluids*, Vol. 44, 2004, pp. 1163–1184. doi:10.1002/fld.694

[17] MacCormack, R. W., “Flow Calculations with Strong Magnetic Fields,” AIAA Paper 2003-3623, 2003.

[18] MacCormack, R. W., “Flow Calculations with Strong Magnetic Effects,” AIAA Paper 2004-0318, 2004.

[19] MacCormack, R. W., “Evaluation of the Low Magnetic Reynolds Approximation for Aerodynamic Flow Calculations,” AIAA Paper 2005-4780, 2005.

[20] MacCormack, R. W., “Simulation of Hypersonic Flow with Strong Magnetic Field Interaction,” AIAA Paper 2006-0970, 2006.

[21] MacCormack, R. W., “Simulation of Hypersonic Flow About an Air Vehicle with Strong Magnetic Field Interaction,” AIAA Paper 2006-3232, 2006.

[22] MacCormack, R. W., “Numerical Simulation of Aerodynamic Flow Within a Strong Magnetic Field with Hall Current and Ion Slip,” AIAA Paper 2007-4370, 2007.

[23] Shang, J. S., Canupp, P. W., and Gaitonde, D. V., “Computational Magneto-Aerodynamic Hypersonics,” AIAA Paper 1999-4903, 1999.

[24] Gaitonde, D. V., and Poggie, J., “Simulations of Magnetogasdynamic Flow Control Techniques,” AIAA Paper 2000-2326, 2000.

[25] Poggie, J., and Gaitonde, D. V., “Magnetic Control of Hypersonic Blunt Body Flow,” AIAA Paper 2000-0452, 2000.

[26] Poggie, J., and Gaitonde, D. V., “Magnetic Control of Flow Past a Blunt Body: Numerical Validation and Exploration,” *Physics of Fluids*, Vol. 14, No. 5, May 2002, pp. 1720–1731. doi:10.1063/1.1465424

[27] Bityurin, V. A., Bocharov, A. N., Lineberry, J. T., and Suchomel, C., “Studies on MHD Interaction in Hypervelocity Ionized Air Flow Over Aero-Surfaces,” AIAA Paper 2003-4303, 2003.

[28] Bityurin, V. A., Bocharov, A. N., and Lineberry, J. T., “MHD Flow Control in Hypersonic Flight,” AIAA Paper 2005-3225, 2005.

[29] Damevin, H. M., and Hoffmann, K. A., “Development of a Runge-Kutta Scheme with Total Variation Diminishing for Magneto-gasdynamics,” *Journal of Spacecraft and Rockets*, Vol. 39, No. 4, July–Aug. 2002, pp. 624–632.

[30] Damevin, H. M., and Hoffmann, K. A., “Numerical Simulations of Magnetic Flow Control in Hypersonic Chemically Reacting Flows,” *Journal of Thermophysics and Heat Transfer*, Vol. 16, No. 4, Oct.–Dec. 2002, pp. 498–507.

[31] Khan, O. U., Hoffmann, K. A., and Dietiker, J. F., “Validity of Low Magnetic Reynolds Number Formulation of Magnetofluiddynamic,” AIAA Paper 2007-4374, 2007.

[32] Hoffmann, K. A., and Chiang, S. T., *Computational Fluid Dynamics*, 4th ed., EES, Wichita, KS, Vol. 2, 2000.

[33] Khan, O. U., Hoffmann, K. A., and Dietiker, J. F., “Computational Aspects of High Speed Flows with Applied Magnetic Field,” *IEEE Transactions on Magnetics*, Vol. 42, No. 3, March 2006, pp. 389–397. doi:10.1109/TMAG.2005.858289

I. Boyd
*Associate Editor*